Spectroscopic study of neon emission and retention in the Tore Supra ergodic divertor

R. Guirlet [a,*], J. Hogan [b], Y. Corre [a], C. De Michelis [a], A. Escarguel [a], W. Hess [a], P. Monier-Garbet [a], B. Schunke [a]

[a] *Association Euratom-CEA sur la Fusion contrôlée, C.E. Cadarache, 13108 St-Paul-lez-Durance, France*
[b] *Oak Ridge National Laboratory, Fusion Energy Division, USA*

Abstract

In order to assess the capability of the Tore Supra ergodic divertor (ED) to retain impurities in the low confinement edge region, spectroscopic observations of a divertor neutraliser plate are reported. The neutral neon density is deduced from these measurements; it increases strongly (up to 1.5×10^{17} m^{-3} per injected Pa l) when the plasma approaches detachment. The central neon density is approximately independent of the plasma edge conditions. A 2D model confirms the relatively weak measured dependence of the neutral neon penetration on edge electron density and temperature. Comparison of BBQ (3D scrape-off layer Monte-Carlo code) results with 1D impurity radial transport modelling suggests a possible mechanism for the observed weak dependence of core content on edge impurity influx: enhanced exchange between the ergodized layer of the core and the neutraliser region. © 2001 Elsevier Science B.V. All rights reserved.

Keywords: Divertor material; Impurity; Plasma–material interaction

1. Introduction

Impurity injection [1,2], particularly neon [3], has often been used to reduce the heat load on the plasma facing components. The effectiveness of the Tore Supra ergodic divertor (ED) to retain impurities in a low confinement region at the plasma edge is a key point for its comparison with X-point divertors. To quantitatively assess this problem, we have used a series of neon-seeded plasmas in a wide range of plasma parameters. The neutral sources on an ED neutraliser plate (NP) have been observed and compared to the bulk impurity content. The experiments and diagnostics are described in Section 2. Section 3 is devoted to the spectroscopic measurement analysis. In Section 4, the ad hoc 2D model and the BBQ 3D code results are presented.

2. Experiments and diagnostics

The standard divertor configuration has been adopted for most pulses used in this study, namely plasma current 1.45 MA, toroidal field 3.1 T, major radius 2.39 m, and minor radius 77.5 cm. In all pulses, after a 0.1 s long neon puff (between 15 and 30 Pa l), a density ramp was performed by deuterium gas injection, allowing to explore the low and high recycling regimes. Three series of pulses have been studied: (1) ohmic heating, $I_{ED} = 45$ kA (maximum perturbation, corresponding to $(\delta B_{ED}/B_{total})_{max} \approx 10^{-3}$); (2) ohmic heating, $I_{ED} = 10$ kA; (3) 1–2 MW ICRH, $I_{ED} = 45$ kA. The n_e^{NP} and T_e^{NP} ranges corresponding to the three series are shown in Fig. 1. When not specified, the study is based on the first series of pulses.

The six ED modules are equipped with seven NPs each, distributed poloidally on the module. In ED configuration plasmas, the whole set of NPs withstands about half of the total particle/heat outflux from the plasma. The best diagnosed NPs are (in the midplane) made of four parallel B$_4$C-coated, actively cooled fingers, on which the field lines connect with an angle of

---

* Corresponding author. Tel.: +33-4 42 25 38 85; fax: +33-4 42 25 49 90.

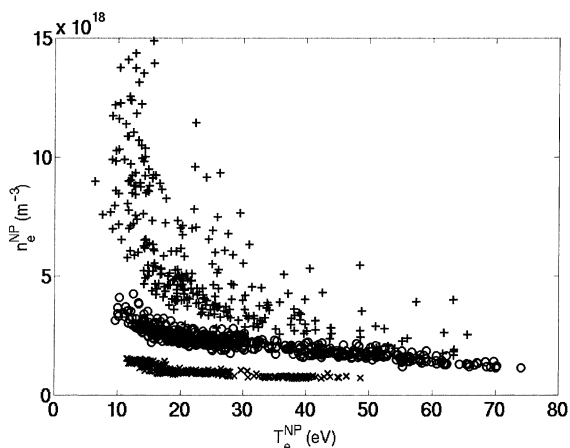*E-mail address:* guirlet@drfc.cad.cea.fr (R. Guirlet).

Fig. 1. Trajectory in the (T_e^{edge}, n_e^{edge}) plane of each of three series of pulses performed for this study (o: ohmic pulses, $I_{ED} = 45$ kA; ×: ohmic pulses, $I_{ED} = 10$ kA; +: 1–2 MW ICRH, $I_{ED} = 45$ kA).

approximately 10°. The fingers are separated by vents designed to pump the particles out of the plasma, terminated by V-shaped notches on which the field lines impinge with a direction close to normal. A set of four in situ optical fibres (called NP fibres in the following), equipped with telescopes embedded in the passive part of a midplane NP, are connected to a visible range spectrometer (Fig. 2). They provide four radial displaced lines of sight in front of the NP. The approximate diameter of the lines of sight is 1–2 cm. An additional in situ fibre views the emitting region of the NP from a top port of the machine, with an angle of 63° with respect to the NP plane. This line of sight (called top line of sight in the following) has been used essentially for Doppler shift measurements. All lines of sight are absolutely calibrated.

On the same NP, electron density and temperature measurements are performed by a domed Langmuir probe installed on the NP plane between two fingers (see Fig. 2). The impurity content in the confined plasma is
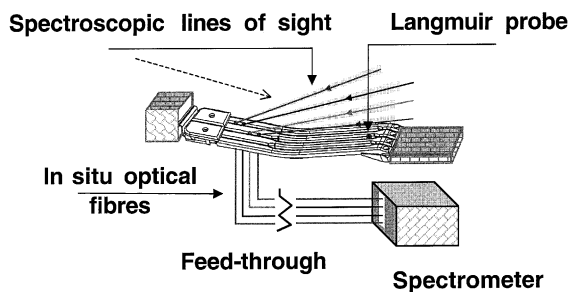

Fig. 2. Diagnostic setup on a midplane NP. The dashed line shows the approximate direction of the magnetic field.

evaluated by using an absolutely calibrated grazing incidence XUV spectrometer with a fixed, equatorial line of sight. The Lyα line brightnesses of the main impurity (intrinsic C, O and injected neon) hydrogen-like ions are measured.

3. Measurements of neon density

3.1. Neon density and emission velocity on the neutraliser plate

We estimate the neutral neon density on the NP from the Ne I 585.2 nm line observed by the fibre closest to the NP. The BBQ code (see below) shows that the Ne I line emissivity $\epsilon_{Ne\ I}$ is approximately uniform along the line of sight; the Ne I line brightness is therefore assumed to be proportional to the neutral neon density. Knowing n_e^{NP} and T_e^{NP} allows to determine the photon emissivity coefficient (PEC), using the collisional-radiative model included in the ADAS atomic data package [4]. The neutral neon density $n_{Ne\ 0}$ is plotted on Fig. 3 as a function of T_e^{NP}. It shows a sharp increase as T_e^{NP} is decreased down to about 12 eV, the plasma being still attached to the divertor plates. This increase is of the same order on all fibres, showing that the neutral neon distribution in the NP vicinity does not change.

At lower divertor perturbation ($I_{ED} = I_{ED}^{max}/4.5$), the same trend is found, although the absolute values of neutral neon density are lower by about a factor 0.7. The minimum neon densities are measured in ICRH scenarios. However, the dominant parameter seems to be T_e^{NP}. For the ohmic pulses, the wavelength shift between the top line of sight and the NP lines of sight (almost
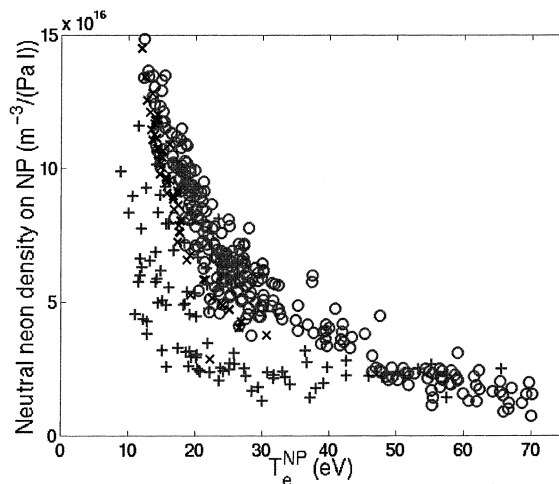

Fig. 3. Neutral neon density as deduced from the Ne I line brightness and the local density and temperature measurements (same symbols as Fig. 1).

parallel to the NP, and thus used as a wavelength reference) has been used to determine the average neutral velocity v_0^{meas}, assuming a cosine angle distribution for the neon atoms emitted from the NP. At large T_e^{NP} values, we find $v_0^{meas} = 615$ m/s, which corresponds to thermal emission at 500 K. When T_e^{NP} is decreased, v_0^{meas} increases up to 3700 m/s at $T_e^{NP} = 25$ eV (and then levels off), indicating the existence of a fast atom population. The relative contribution and the emission energy of these fast atoms cannot be determined unambiguously from this single measurement. However, assuming a fast neutral energy in the range 10–20 eV, consistent with TRIM [5] predictions for fast reflected neutral neon, we estimate the ratio of the fast to slow atom fluxes to lie in the range 0.4 (low ED perturbation, low T_e^{NP}) to 3.3 (high ED perturbation, low T_e^{NP}). This is considerably larger than the particle reflection coefficient calculated by TRIM. This can be due to the complex geometry of the NP, resulting in a varying angle of the incident flux on the material surfaces.

3.2. Neon density in the core

The C VI, O VIII and Ne X Lyα line brightnesses are measured with the absolutely calibrated XUV spectrometer. Charge exchange spectroscopic measurements [6] are then used, together with a 1D impurity transport model, to determine the position of each ion emission layer and the density ratio between the emission layer and the plasma centre for the three species. Knowing the electron density and temperature at the emission location, and thus the PEC, the central impurity density for the main three species can be deduced. The Z_{eff} measurement is then used to check the calculated densities. While the intrinsic impurity densities show, as reported in [7], a decrease as T_e^{NP} decreases, the central neon density is approximately constant (about 4×10^{16} m^{-3}/ Pa l) in all edge conditions. As a consequence, the compression factor increases in the same proportion as the NP neon density when the plasma is led from the low recycling regime ($T_e^{NP} \approx 50$ eV) to the high recycling regime ($T_e^{NP} \approx 20$ eV).

4. Modelling

4.1. Neutral neon distribution calculation with a 2D model

A 2D model calculating the neutral neon density has been used to interpret the results reported in Section 3.1. The plane chosen for this calculation extends in the direction parallel to the NP fingers and in the radial direction. We do not model the V-notches, on which the incident flux is larger, since their surface is much smaller than that of the fingers. The electron density has been measured to decay exponentially at the plasma edge with

a radial e-folding length of 3 cm [8], and the Langmuir probe measurement on the NP observed with the fibres is used as a reference. For the electron temperature, we use the 3D code MASTOC [9] which calculates the magnetic field configuration in the ergodised region, and from this, an electron temperature mapping in the working plane.

The second step is the description of the neutral neon emitted flux Φ_{Ne0} and of its propagation in the (T_e, n_e) mapping previously calculated. Due to the almost total recycling property of neon, Φ_{Ne0} on the NP can be assumed to be proportional to the incident neon flux, which itself is assumed to have the same spatial distribution as the incident deuterium flux. A $n_e^{NP} \times (T_e^{NP})^{1/2}$ dependence is thus assumed for Φ_{Ne0}. At each emission point the neutrals are emitted at a given energy with a cosine angular distribution. They are then propagated using the ionisation rate coefficient provided in ADAS. All modelled cases (various n_e^{NP} and T_e^{NP}, various divertor currents) show a relatively smooth neutral distribution compared to the marked inhomogeneities of T_e, as can be seen in Fig. 4. The model also calculates the neutral penetration depth, defined as the perpendicular distance to the NP plane within which 63% of the neutrals can be found (more or less equivalent to an e-folding length of an exponential decay). Various neutral energies have been used as input to the model. The penetration depth is compared in Fig. 5 to the ionisation length calculated from the local (Langmuir probe) n_e and T_e values. In all cases the model predicts that, despite the wide range of T_e^{NP} and n_e^{NP} values, the penetration depth increases only slightly (by a factor 1.6–2.2) when T_e is decreased, in reasonable agreement with the neon density profiles deduced from the fibres.

4.2. Simulations with the 3D code BBQ

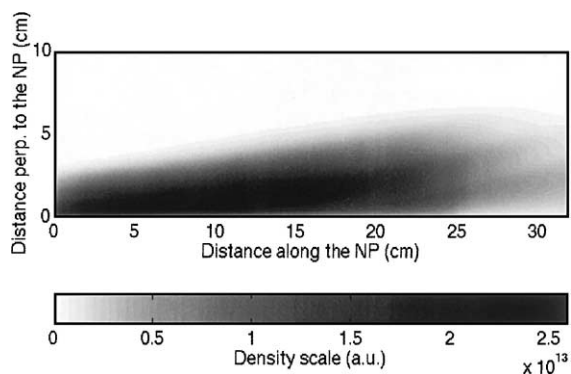BBQ [10] 3D Monte-Carlo neon transport simulations have been made for the NP (with the detailed

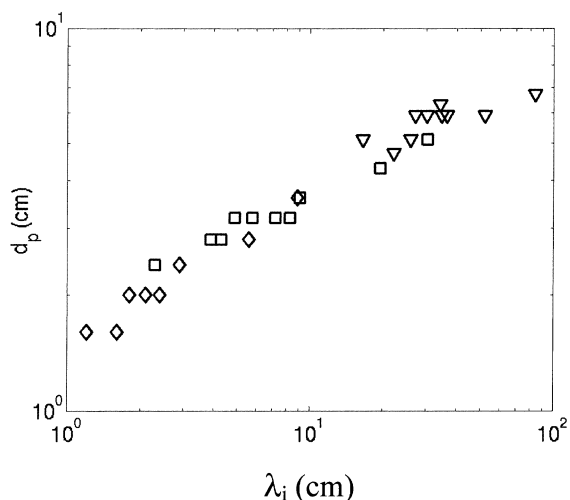Fig. 4. Neutral neon density (in relative units) deduced from the 2D model.

Fig. 5. Penetration depth deduced from 2D modelling as a function of the global ionisation length for various neutral energies: thermal (0.04 eV, diamonds), fast (TRIM, triangles) and measured (squares).

4-needle, 3-notch geometry) (Fig. 6). They show an increased neon penetration (which describes the influx to the ergodised region from the NP) as T_e^{NP} decreases. This accompanies a decrease in the locally re-deposited fraction (Fig. 7). BBQ/MIST calculations are used to match the core neon content using transport coefficients previously 'validated', for shots with CXS measurements of C and Ne profiles. The resulting calculated radial impurity outward flux shows a strong increase in the ergodized region. Recycling impurities will therefore be preferentially expelled from this region towards the NP. There is thus a weaker connection between edge influx and core content than for modes (such as VH-mode or
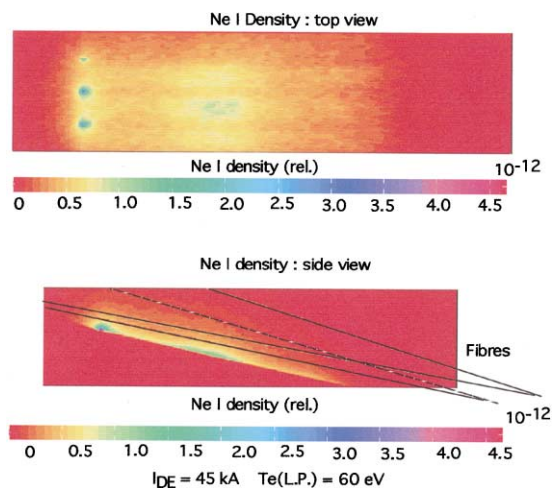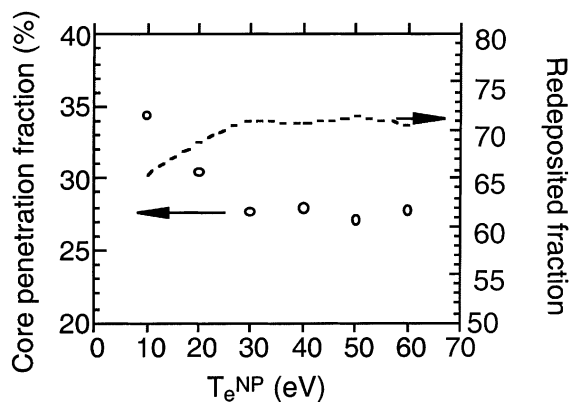

Fig. 6. Neutral neon density calculated by BBQ.

Fig. 7. BBQ calculation of the penetrating (circles) and re-deposited (dashed line) fractions as functions of the NP temperature.

Enhanced Reverse Shear) where the impurities may actually be drawn into the core, rather than expelled. This behaviour is very similar to the effect of ELMs on recycling impurities in H-mode.

5. Conclusion

It has been shown that the neon core content is fairly insensitive to plasma edge conditions, despite the fact that the neutral neon density on the plate varies by a factor of at least 7. This indicates that the core plasma is decoupled from the emission region. This is indeed confirmed by BBQ/MIST calculations, showing that most of the neon does not penetrate further than the divertor region before being transported back onto the NP, due to increased parallel transport at the edge. The use of a 2D model has shown that despite the wide range of edge parameters observed in this study, the neutral neon penetration depth does not vary by more than a factor 2. The neutral neon velocity measurements indicate the existence of two populations: slow neon atoms emitted by the NP at thermal energy ($E_0 \approx 0.04$ eV) and fast reflected atoms. Although the latter relative contribution and energy cannot be unambiguously determined, the measurement does not seem consistent with the TRIM predictions, possibly because of the NP geometry.

References

[1] J. Neuhauser, Plasma Phys. Control. Fus. 37 (1995) A37.
[2] T. Ishijima et al., Plasma Phys. Control. Fus. 41 (1999) 1155.
[3] N. Richard et al., J. Nucl. Mater. 241–243 (1997) 760.
[4] H.P. Summers, JET internal report JET-IR(94)06.
[5] W. Eckstein, J. Nucl. Mater. 248 (1998) 1.

[6] W. Hess et al., in: Proceedings of the 26th EPS International Conference on Controlled Fusion and Plasma Physics, Prague 2000.

[7] B. Schunke et al., these Proceedings.

[8] J. Gunn et al., Plasma Phys. Control. Fus. 41 (1999) B243.

[9] P. Ghendrih et al., Plasma Phys. Control. Fus. 38 (1996) 1653.

[10] J. Hogan et al., in: Proceedings of the 16th IAEA international conference on plasma physics and controlled fusion research, Montreal 1996, vol. 2, p. 625.